Biointerface Research in Applied Chemistry
Open-Access Journal (ISSN: 2069-5837)

Article
Volume 16, Issue 2 2026, 51
https://doi.org/10.33263/BRIAC162.051

Ultrasonically Synthesized Deep Eutectic Solvents with Additive Engineering: Unraveling an Anomalous Ionic Conductivity Trend and the Paradox of High-Viscosity Potassium Iodide

Pragya Kumar [1,*], Kamlika Banerjee [1], Yogesh Kumar [2], Monika Vikal [3]

[1] School of Sciences, Indira Gandhi National Open University; New Delhi 110068, 210271589@ignou.ac.in (P.K.); kamalika@ignou.ac.in (K.B.);
[2] Department of Physics, ARSD College, University of Delhi, New Delhi 110036, India; ykumar@arsd.du.ac.in (Y.K.);
[3] Department of Zoology, Hansraj College, University of Delhi, Delhi 110007, India; monikavikal@hrc.du.ac.in (M.V.)
* Correspondence: 210271589@ignou.ac.in;

Received: 28.08.2025; Accepted: 15.11.2025; Published: 15.04.2026

Abstract: Efficient electrolytes are crucial for next-generation energy storage systems. Here, a deep eutectic solvent (DES) based on polyethylene glycol (PEG) and zinc chloride ($ZnCl_2$) was synthesized via ultrasonication, and the influence of additives such as acetonitrile (ACN), potassium iodide (KI), and glycerol on its electrochemical performance was examined. Cyclic voltammetry and impedance spectroscopy revealed that the DES–KI system exhibited notably high ionic conductivity (0.052 mS cm^{-1}) and a specific capacitance of 41.6 F g^{-1}. This enhancement is linked to improved ion transport and redox activity within the DES matrix. The findings highlight the tunability of DES-based electrolytes through additive selection, presenting DES–KI as a promising platform for high-performance supercapacitors and other advanced energy storage applications.

Keywords: deep eutectic solvent; PEG–$ZnCl_2$ electrolyte; ionic conductivity; electrochemical performance; potassium iodide.

1. Introduction

The growing demand for sustainable and efficient energy storage technologies has prompted the exploration of alternative electrolytes, especially for supercapacitor (SC) applications. Among these, deep eutectic solvents (DES), composed of biocompatible and biodegradable components, have attracted considerable attention due to their excellent electrochemical stability, tunable physicochemical properties, and environmental safety [1]. Unlike traditional ionic liquids (ILs), which suffer from toxicity and environmental persistence issues [2], DES provide a greener and safer alternative for next-generation energy systems [3,4].

In *SCs*, *DES* offer key benefits such as low volatility, thermal stability, and wide electrochemical windows, which contribute to improved energy and power density along with enhanced safety and lifetime [5–7]. However, their ionic conductivity and viscosity still pose performance limitations. Addressing this challenge, recent studies have demonstrated that *DES*

performance can be significantly improved by incorporating additives and optimizing synthesis routes. For instance, Wang *et al*. [8] developed a DES-based electrolyte for Zn-ion batteries showing improved Coulombic efficiency, while Perry *et al*. [9] achieved template-free electrochemical nanowire deposition using DES, and Fan *et al*. [10] enhanced interfacial lubrication via *DES*-graphene oxide intercalation. Furthermore, Alhanash *et al*. [11] explored symmetry effects in *DES* using tight-binding models, providing theoretical insights into electrolyte behavior.

DES have emerged as a versatile class of green solvents with promising applications in energy storage, catalysis, and electrochemistry. The concept was first introduced by Abbott *et al*. in 2003, who reported melting point depression in a choline chloride–urea system [12]. Generally composed of a hydrogen bond donor (HBD) and a hydrogen bond acceptor (HBA), DES offer flexible compositional design, enabling tailored physicochemical properties for diverse applications. Various synthesis strategies have been developed, each with inherent strengths and limitations. Conventional heating–stirring methods are widely adopted but may lead to impurity formation, particularly when acid-based components are used [13–16]. Alternatives such as vacuum evaporation [17], lyophilization [18,19], grinding [20], and twin-screw extrusion provide better control but require specialized equipment. More recently, ultrasound-assisted synthesis (UAS) has emerged as a green, rapid, and energy-efficient route. Through cavitation and microjet formation, ultrasound enhances hydrogen bonding and homogeneous mixing, lowering energy consumption and improving solvent uniformity [18,21–23]. For instance, ChCl-based DES synthesized via UAS exhibited significantly reduced viscosity and activation energy for viscous flow (50.75 kJ mol^{-1}) compared to heating–stirring (77.90 kJ mol^{-1}) [24]. Comparative studies further showed that UAS consumes the least energy (0.006 kWh mL^{-1}), outperforming microwave-assisted synthesis, which, although fast, demands higher energy input [25]. Grinding and freeze-drying techniques also provide purity advantages by avoiding thermal degradation but are hindered by longer synthesis times and higher equipment requirements [13,26–29]. Overall, ultrasound and grinding approaches are considered particularly favorable for applications requiring stable, low-viscosity, and impurity-free DES formulations [30–32].

In the context of electrochemical energy storage, tailoring DES properties with suitable additives has become an important research focus. KI, ACN, and glycerol have been identified as effective components for enhancing DES-based electrolytes. KI is of particular interest due to its redox-active nature, which contributes to pseudocapacitance and enhances charge storage through reversible iodide redox reactions, thereby improving both capacitance and energy density [33,34]. ACN, when introduced as a cosolvent, reduces viscosity and enhances ionic mobility without significantly disrupting the hydrogen-bonding network, thereby improving overall conductivity [35]. Glycerol, as an HBD, stabilizes DES formation through robust hydrogen bonding, minimizes self-discharge, and strengthens electrode–electrolyte interactions [36]. Additionally, glycerol is environmentally benign and aligns with principles of sustainable chemistry. In contrast, salts such as $FeCl_3$ and $CaCl_2$ are generally avoided due to hydrolysis, side reactions, or precipitation that compromise stability and performance [37,38]. These additive effects collectively demonstrate how compositional tuning can modulate both ionic mobility and electrochemical stability in DES-based systems [39].

The present study focuses on the ultrasound-assisted synthesis of PEG-$ZnCl_2$-based DES and the role of KI, ACN, and glycerol as additives in modulating their electrochemical properties. Electrochemical characterization was carried out using stainless steel and activated

carbon electrodes. We hypothesize that the introduction of targeted additives can simultaneously enhance ionic conductivity and capacitance by optimizing the conductivity–viscosity balance within PEG–$ZnCl_2$-based DES electrolytes. This hypothesis-driven approach aims to establish a mechanistic understanding of additive-induced enhancements and guide the rational design of DES for high-performance supercapacitors and related energy storage applications.

2. Materials and Methods

2.1. Materials.

All chemicals used in this study, including their CAS numbers, purities, and suppliers, are listed in Table 1. Polyethylene glycol (PEG-200) and $ZnCl_2$ were selected as the HBD and HBA, respectively, for DES synthesis. KI, glycerol (GLY), and ACN were incorporated as additives. Deionized water (18.2 MΩ·cm) was used throughout the experiments.

Table 1. Detailed information about the chemicals and reagents used.

Chemical name	CAS No	Purity	Brand name
$ZnCl_2$	7646-85-7	97%	Fisher Scientific
PEG-200	25322-68-3	-	Sigma Aldrich
Glycerol	56-81-5	99.5%	Sisco Research Laboratories Pvt. Ltd.
KI	7681-11-0	-	FINAR
ACN	75-05-08	99.9 %	Sigma Aldrich
Activated charcoal granular	7440-44-0	Extra pure	Loba Chemie Pvt. Ltd.
Acetylene black/ carbon black	1333-86-4	99.9%	Thermo Fisher Scientific
PVDf-HFP	9011-17-0	99.99%	Sigma Aldrich
Acetone	67-64-1	>99%	Qualigens

2.2. Synthesis of DES electrolytes.

A DES was synthesized by mixing PEG-200 and $ZnCl_2$ in a 1:3 molar ratio in a glass beaker. The mixture was placed in a water bath ultrasonicator maintained at 60°C to ensure uniform heating and efficient dissolution. KI, GLY, and ACN were each introduced at 0.5 wt% to tailor electrochemical properties. The mixture was sonicated for 1.5 h, with manual stirring every 30 min using a glass rod to promote homogeneity. Formation of a stable and transparent DES was confirmed visually (Figure 1). Each synthesis was repeated three times to confirm reproducibility, and observed variations in viscosity and conductivity remained within ±3%. The DES samples were stored in sealed containers at room temperature to prevent moisture uptake. The ultrasound-assisted synthesis approach was selected for its demonstrated ability to reduce viscosity, enhance homogeneity, and improve ionic transport [40–54].

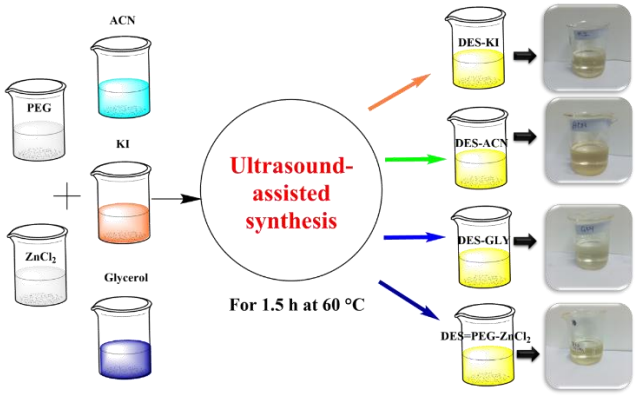

Figure 1. Ultrasound-assisted synthesis of $ZnCl_2$-based DESs using PEG with additives, KI, ACN, and glycerol, at 60°C for 1.5 h; photographs show homogeneous DESs obtained after sonication.

2.3. Preparation of activated carbon electrodes.

Activated carbon (AC) electrodes were fabricated by mixing AC (8 wt%) with acetylene black (1 wt%) and PVDF–HFP binder (1 wt%). The mixture was dispersed in acetone to form a slurry, which was uniformly coated onto pre-cleaned aluminum foil (current collector) using the doctor-blade method. The electrodes were dried at 60°C for 4 h, cut into circular discs (1.2 cm diameter), and mechanically pressed to improve contact and reduce internal resistance. The active material loading was maintained between 2.0–2.5 mg per electrode with a variation below ±0.05 mg.

2.4. Physicochemical characterization.

Elemental composition: A Shimadzu EDX-7200 energy-dispersive X-ray fluorescence (EDXRF) spectrometer was used to analyze elemental composition using the solution-screening method.

Functional group analysis: Fourier transform infrared (FTIR) spectra were obtained using a PerkinElmer spectrometer equipped with KBr optics and a diamond ATR accessory, with a resolution of 0.5 cm^{-1} over the range 4000–400 cm^{-1}. Spectra were analyzed to identify hydrogen bonding, Zn^{2+}–PEG coordination, and additive effects.

Thermal analysis: Thermogravimetric analysis (TGA) was performed using a TGA/DSC 3+ system (METTLER TOLEDO) in the range of 30–500°C under N_2 atmosphere. Differential scanning calorimetry (DSC) was carried out using a DSC7000X (Hitachi) from −10 to 400°C at 10°C·min^{-1} under N_2 flow (100 mL·min^{-1}).

Conductivity: Ionic conductivity was measured at room temperature using a TOSHCON–TOSHNIWAL TC17 conductivity meter, calibrated with standard KCl solutions (0.01-1 M).

Viscosity: Viscosity was measured using a Labman LMDV-200 digital viscometer with an L28 spindle at 30 rpm, maintained at 24.8 ± 0.2°C.

2.5. Electrochemical characterization.

Electrochemical performance was evaluated using a PalmSens4 potentiostat in a two-electrode setup.

Cyclic voltammetry (CV): Performed at scan rates of 10 and 20 mV·s^{-1}. Stainless steel (SS) electrodes were used within −0.5 to 1.0 V to probe redox stability, while AC electrodes were scanned from 0 to 2.0 V to assess capacitive behavior.

Electrochemical impedance spectroscopy (EIS): Conducted using SS electrodes over the frequency range of 0.01 Hz to 1 kHz to evaluate ionic conductivity and charge-transfer resistance via Nyquist plots.

All electrochemical tests were conducted at room temperature. Each experiment was repeated three times to ensure reproducibility.

3. Results and Discussion

3.1. ED-XRF analysis.

ED–XRF was used to determine the elemental composition of the DES formulations and verify additive incorporation. Quantitative data were analyzed to correlate elemental ratios with electrochemical behavior and to evaluate how the addition of cosolvents or salts altered

zinc coordination. Figure 2(a–d) presents the ED–XRF spectra of the DES systems, showing characteristic emission lines from zinc, chloride, and other trace elements. To complement these spectra, Table 2 summarizes the quantitative elemental composition and the principal ZnKα emission peak characteristics for each formulation. These spectral shifts are particularly informative, as they reflect electronic structural modifications resulting from additive incorporation and solvent interactions within the DES matrix.

The baseline $ZnCl_2$–PEG DES displayed dominant Zn and Cl peaks, confirming successful complexation of Zn^{2+} within the PEG network. Trace elements (K, Ca, Cu <0.1 %) were negligible and below interference thresholds [55]. Incorporation of KI introduced distinct K peaks (2.45 %) and reduced Zn/Cl intensities, indicating effective interaction of KI with the $ZnCl_2$–PEG matrix. The small ZnKα shift (−0.03 keV) suggests modification of zinc's coordination environment due to partial iodide substitution or complexation. The glycerol-based DES exhibited decreased Zn and Cl contents and a high-water content (76.46 %), consistent with glycerol's hygroscopic nature. The minor spectral shift (−0.02 keV) supports altered solvation and possible ion aggregation. The ACN-based DES maintained near-identical Zn and Cl content but lower water levels, indicating improved ion dissociation and reduced clustering. Minimal peak shift (+0.01 keV) and reduced impurity levels (<0.01 %) reflect strong solvent coordination and enhanced compositional uniformity.

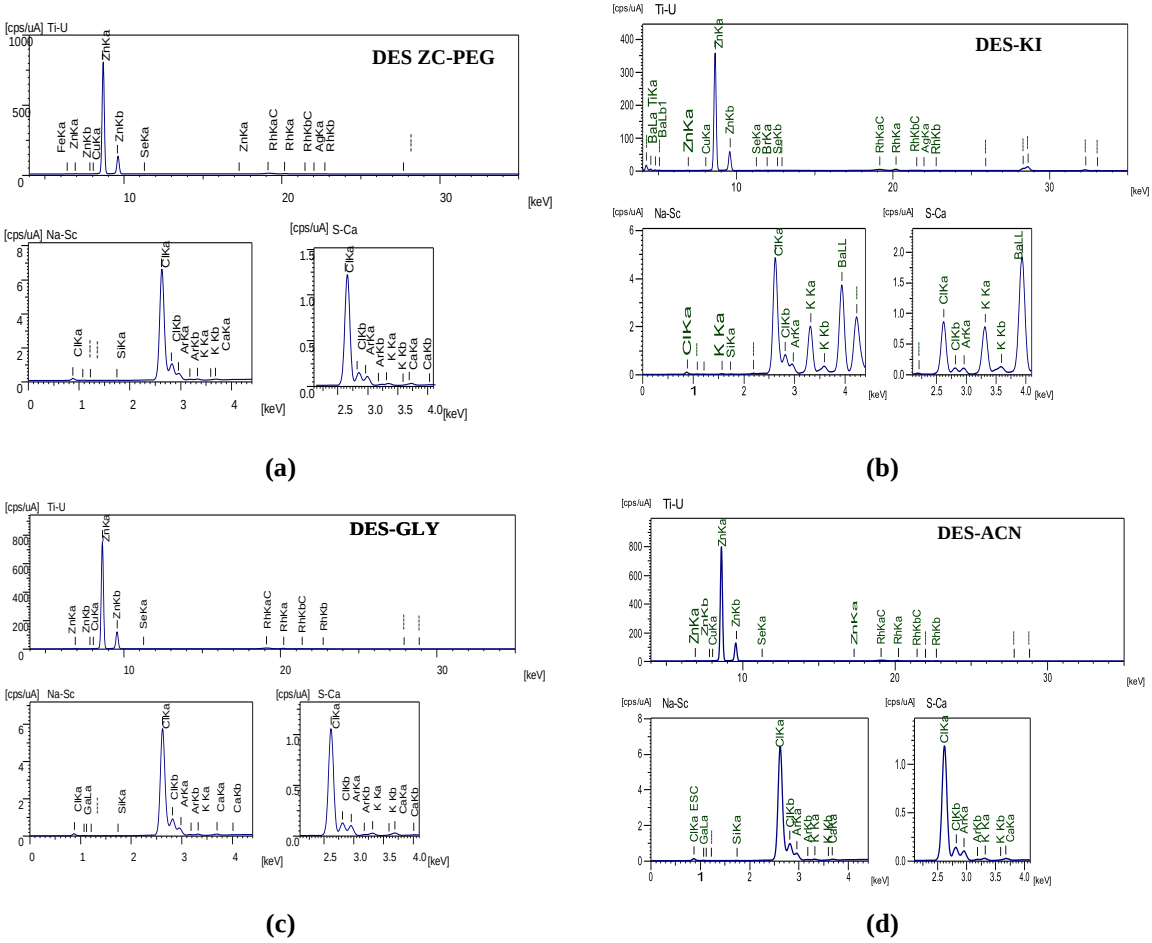

Figure 2. ED–XRF spectra of $ZnCl_2$-based DES systems showing elemental composition and additive effects: **(a)** ED–XRF spectrum of the baseline $ZnCl_2$–PEG DES showing Zn and Cl peaks; **(b)** DES–KI confirming potassium incorporation; **(c)** DES–Gly displaying reduced Zn and Cl content and higher water uptake; **(d)** DES–ACN exhibiting comparable Zn and Cl content with minimal impurities, confirming additive-dependent compositional variation.

Table 2. Elemental composition of PEG–$ZnCl_2$-based DES systems.

Sample	Zn (%)	Cl (%)	K (%)	Cu (%)	Ca (%)	H_2O (%)	Major Peak (ZnKα, keV)	Observed Shift (ΔkeV)
$ZnCl_2$–PEG (Base DES)	13.313	14.543	–	0.014	0.045	74.982	8.64	–
DES–KI	3.9810	8.4990	2.45	–	–	72.420	8.61	0.03
DES–Glycerol	10.969	12.144	–	–	–	76.458	8.62	0.02
DES–ACN	13.313	14.543	–	<0.01	–	71.684	8.65	0.01

[1]*ΔkeV* values indicate minor shifts relative to the base DES, reflecting subtle differences in Zn coordination environments.

3.2. FT-IR analysis.

FT-IR spectroscopy was employed to elucidate the structural interactions and intermolecular bonding within the synthesized DESs composed of $ZnCl_2$ and PEG, incorporating additives such as glycerol, KI, and ACN. Comparative analysis of the DES spectra with those of individual components enabled identification of hydrogen bonding, ionic coordination, and functional group interactions that underpin DES formation. The reference spectra of the individual components (Figure 3a-i to 3a-v) provide the baseline for interpreting the DES systems. The ACN spectrum (Figure 3a-i) shows a distinct nitrile (C≡N) stretching band at ν = 2252.68 cm^{-1}, along with C–H stretching peaks at ν = 2944.45 and 2292.58 cm^{-1}. KI (Figure 3a-ii) exhibits characteristic O–H stretching at ν = 3431.94 cm^{-1} and a water-bending mode at ν = 1619.50 cm^{-1}, confirming hydration due to its hygroscopic nature. The glycerol spectrum (Figure 3a-iii) presents intense O–H stretching at ν = 3405.09 cm^{-1} and C–O bands at ν = 1060.70, 1248.24, and 1350.27 cm^{-1}, indicative of extensive hydrogen bonding. PEG–based $ZnCl_2$ reference (Figure 3a-iv and 3a-v) shows broad O–H bands near ν = 3371.80 cm^{-1} and Zn–Cl stretching at ν = 1412.53 and 626.33 cm^{-1}, confirming hydration and metal–halide ionic character. Figure 3b compares the spectra of the formulated DES systems, illustrating additive-induced structural modifications. Quantitative analysis of the major vibrational bands and their corresponding shifts (Δν) relative to reference compounds is summarized in Table 3. These data highlight key interactions—particularly O–H red-shifts and Zn–O/Zn–Cl coordination—responsible for the establishment of a stable, ionically conductive framework.

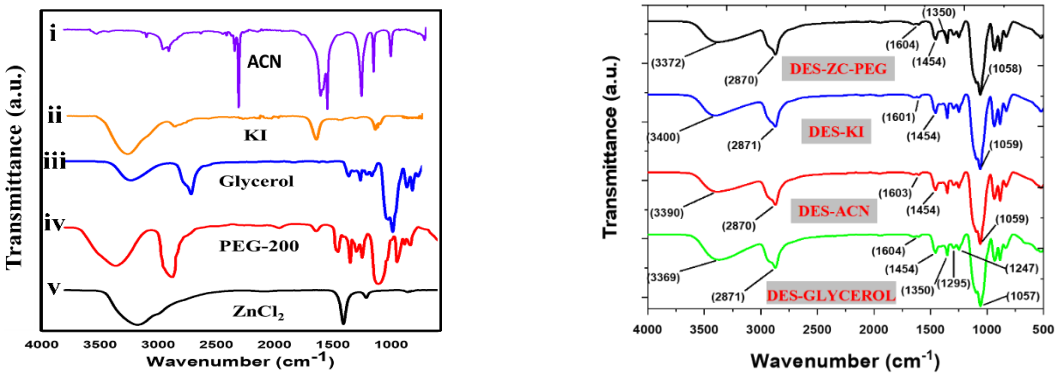

Figure 3. (a) FTIR spectra of reference materials: **(i)** ACN, **(ii)** KI, **(iii)** glycerol, **(iv)** PEG-200, and **(v)** $ZnCl_2$, showing characteristic vibrational bands for O–H, C–O, C≡N, and Zn–Cl functional groups. **(b)** FTIR spectra of synthesized DES systems based on $ZnCl_2$–PEG, illustrating the formation of hydrogen bonds and coordination between Zn^{2+} and donor groups. Spectral shifts upon the addition of glycerol, KI, and ACN confirm modified intermolecular interactions and stable eutectic formation.

The base $ZnCl_2$–PEG DES (Figure 3b) exhibited strong O–H stretching near 3390.78 cm^{-1} and characteristic Zn–O and Zn–Cl vibrations at 883.60 and 522.23 cm^{-1}, confirming Zn^{2+} coordination with PEG's ether oxygens to form a stable ionic network. Incorporation of glycerol resulted in broadened and red-shifted O–H stretching ($\Delta\nu \approx 21$ cm^{-1}), reflecting enhanced hydrogen bonding and increased dipolar interactions. For the KI-modified system, a further O–H red-shift ($\Delta\nu \approx 32$ cm^{-1}) and intensified C–O bands indicated iodide integration within the hydrogen-bonding matrix, promoting stronger ionic interactions and potentially improved ion transport. In the ACN-based DES, the nitrile stretching band shifted from 2252.68 to 1603.53 cm^{-1}, suggesting weak Zn^{2+}–nitrile coordination without disrupting the overall DES structure.

Table 3. Key FT-IR absorption bands and peak shifts (Δν) of DES systems.

DES sample	Major vibrational modes	Assigned functional group	ν (cm^{-1})	Δν (cm^{-1})*	Conclusion
KI	O–H stretch	Hydration / H-bonded OH	3431.94	–	Hygroscopic water presence
Glycerol	O–H stretch / C–O stretch	H-bonded alcohol	3405.09 / 1060.70	–	Strong intramolecular H-bonding
ACN	C≡N stretch	Nitrile group	2252.68	–	Polar nitrile vibration
$ZnCl_2$	Zn–Cl / Zn–O stretch	Metal–halide / hydrated Zn	1412.53 / 626.33	–	Ionic coordination features
Base DES ($ZnCl_2$–PEG)	O–H / C–H / Zn–O / Zn–Cl	Hydrogen bonding, coordination	3390.78 / 2870.98 / 883.60 / 522.23	15.3 (O–H)	Formation of Zn–PEG complex
DES–Glycerol	O–H / C–O / Zn–O	H-bonding enhancement	3369.83 / 1057.28 / 1350.39	21.3 (O–H)	Increased H-bond density
DES–KI	O–H / C–O	I^- interact with polyols	3400.12 / 1059.13 / 1350.30	31.8 (O–H)	Iodide integration into the network
DES–ACN	O–H / C≡N / Zn–O / Zn–Cl	Weak Zn–nitrile coordination	1603.53 / 2871.58 / 522.21	10.0 (C≡N)	Retains DES core structure

[1]Δν calculated relative to corresponding reference compound peaks.

3.3. Viscosity.

Viscosity is a key physicochemical parameter that dictates the processability and electrolyte performance of DESs, influencing ionic mobility, heat transfer, and thermal responsiveness [56, 57]. The viscosities of $ZnCl_2$–PEG-based DESs with glycerol, KI, and ACN were measured (Figure 4) to assess the influence of hydrogen bonding and ionic interactions. The base $ZnCl_2$–PEG DES showed a moderate viscosity of ~530 mPa·s, reflecting a balance between hydrogen bonding (–OH···Zn^{2+}) and Zn^{2+} coordination with oxygen/chloride, which provides both structural stability and fluidity. Glycerol incorporation, despite strengthening the hydrogen-bond network (O–H stretch shifted to 3369.83 cm^{-1}), slightly reduced viscosity to ~515–518 mPa·s, indicating integration into the DES without excessive rigidity. KI addition markedly increased viscosity to ~914–919 mPa·s. This rise is attributed to additional hydrogen bonding from water absorbed by hygroscopic KI and strong I^-···Zn^{2+} ionic interactions, which enhance structural ordering and restrict molecular mobility. Conversely, ACN reduced viscosity to ~360–361 mPa·s by coordinating via its nitrile group with Zn^{2+}, increasing molecular spacing and weakening intermolecular associations while preserving the DES framework. The relative hydrogen bonding strength follows: DES–KI > DES–Gly > Base DES > DES–ACN. FTIR data corroborate this ranking, directly linking bonding interactions to viscosity behavior.

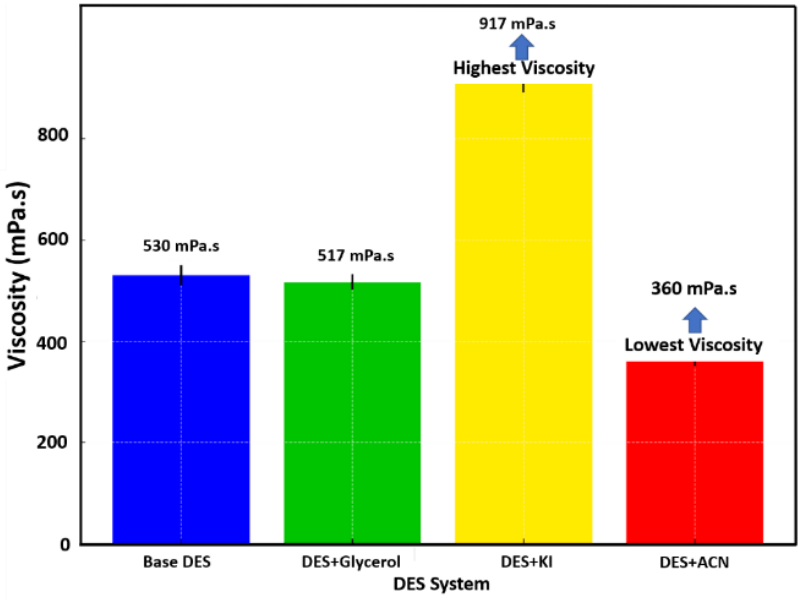

Figure 4. Viscosity comparison of $ZnCl_2$–PEG-based DESs with different additives. DES-KI exhibited the highest viscosity (917 mPa·s) due to ion association, whereas DES-ACN showed the lowest viscosity (360 mPa·s), attributed to enhanced ion mobility and reduced intermolecular interactions.

3.4. Thermal analysis.

Thermal analysis was performed to assess the decomposition behavior and thermal stability of the synthesized DESs, critical parameters for energy storage systems operating across wide temperature ranges [14, 52]. The onset decomposition temperature (T_{onset}) from TGA was determined via the extrapolation method reported previously [58, 59]. Both DSC and TGA results are shown in Figure 5a. DSC analysis revealed high T_{onset} values for all formulations, indicating robust thermal stability (Figure 5b). DES–Gly displayed the highest DSC T_{onset} (380.74°C), followed by DES–KI, DES–ACN, and the base $ZnCl_2$–PEG (ZC–PEG) DES. No melting or freezing transitions were detected, likely due to the absence of measurements at sufficiently low temperatures. TGA results corroborated the DSC trends while providing additional insights into mass loss behavior.

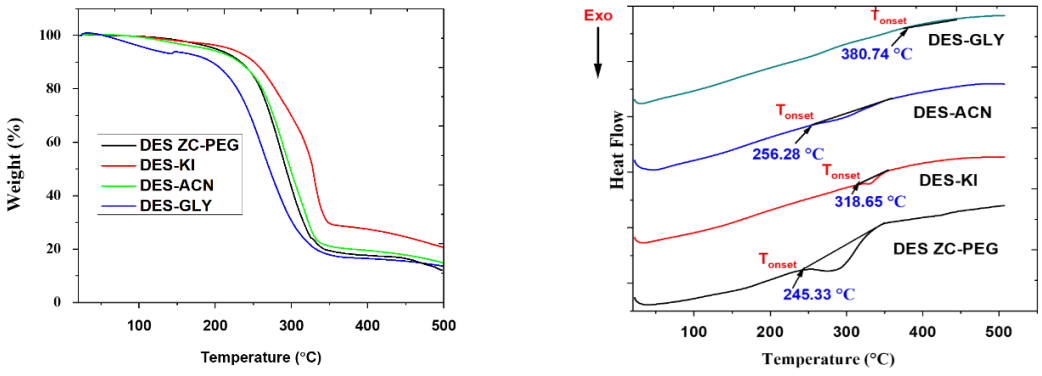

Figure 5. (a) TGA plots of synthesized DESs and DESs with additives showing single-step thermal degradation and high stability; **(b)** DSC plots illustrating onset decomposition temperatures and the absence of phase transitions, confirming strong intermolecular interactions.

As expected, TGA T_{onset} values were slightly lower than DSC values, reflecting TGA's greater sensitivity to early volatilization and partial decomposition. The highest TGA T_{onset} was observed for DES–Gly (189.60°C), followed by DES–KI (240.85°C),

DES–ACN (214.77°C), and ZC–PEG (~245°C). All samples exhibited single-step decomposition, indicating strong intermolecular interactions and homogeneous eutectic formation. Collectively, the high decomposition temperatures, absence of complex phase transitions, and single-step degradation confirm excellent thermal stability and structural integrity across all DES systems. These properties, driven by strong hydrogen-bond donor–acceptor (HBD–HBA) interactions, make them promising for high-temperature electrochemical applications. Table 4 summarizes the TGA and DSC onset decomposition temperatures (T_{onset}) for the DES systems. The consistently high thermal stability confirms that all formulations can withstand elevated operational temperatures without significant structural degradation.

Table 4. Thermal decomposition onset temperatures (T_{onset}) obtained from TGA and DSC analyses.

Sample	DSC T_{onset} (°C)	TGA T_{onset} (°C)	Decomposition profile	Conclusion
ZC–PEG (Base DES)	245.33	245.00	Single-step	Stable coordination between Zn^{2+} and PEG
DES–Gly	380.74	189.60	Single-step	Strongest H-bonding; highest thermal resilience
DES–KI	318.65	240.85	Single-step	Iodide enhances ionic stability and bonding strength
DES–ACN	256.28	214.77	Single-step	Moderate stability due to ACN–Zn^{2+} coordination

3.5. Cyclic voltammetry.

CV was used to evaluate the electrochemical behavior of the synthesized DES systems with stainless steel electrodes over a potential window of –0.5 to 1.0 V at scan rates of 10 mV s^{-1} and 20 mV s^{-1} (Figure 6a–b). At 10 mV s^{-1}, the base PEG–$ZnCl_2$ DES exhibited the broadest current response with pronounced oxidation peaks, indicative of strong redox activity and good electrochemical reversibility. Its specific capacitance was calculated as 24.64 F g^{-1}, reflecting moderate charge storage capability. The DES–KI sample showed weaker redox features and lower current response, likely due to slower electron-transfer kinetics or less favorable electrode–electrolyte interactions. In contrast, DES–Gly displayed more defined redox peaks and higher current density than DES–KI, suggesting improved charge transfer and stronger interfacial interactions. DES–ACN exhibited higher oxidation currents than both DES–Gly and DES–KI, possibly due to Zn^{2+}-nitrile coordination, which may enhance ion mobility and redox accessibility. At 20 mV s^{-1} (Figure 6b), PEG–$ZnCl_2$ maintained distinct redox peaks and consistent current density, confirming its electrochemical stability. DES–KI remained the least active, whereas DES–Gly retained moderate activity with broader peaks. DES–ACN exhibited a sharper oxidation peak and increased current density, indicating improved electron kinetics at higher scan rates. The electrochemical stability window (ESW) was determined from the potential range preceding electrolyte breakdown [60]. DES–KI displayed the narrowest ESW (~1.2 V; –0.4 to 0.8 V), DES–Gly extended slightly to ~1.3 V (–0.3 to 1.0 V), while PEG–$ZnCl_2$ and DES–ACN exhibited broader ESWs (~1.5 V) spanning –0.5 to 1.0 V and –0.4 to 1.1 V, respectively, suggesting greater stability for wider voltage operation. CV measurements with activated carbon electrodes (Figure 6c–d) provided additional insight into capacitive behavior. The near-rectangular voltammograms indicated quasi-reversible redox processes characteristic of electrochemical double-layer capacitors (EDLCs). Among the tested systems, DES–KI (green curve) showed the highest current response and largest enclosed area, corresponding to a specific capacitance of 41.60 F g^{-1}, attributed to enhanced ionic conductivity from iodide ions. DES–Gly (red curve) achieved 38.48 F g^{-1}, supported by its extensive

hydrogen-bonding network. DES–ACN (blue curve) exhibited a moderate capacitance of 25 F g^{-1}, benefiting from improved ionic mobility through Zn^{2+}–ACN coordination, while PEG–$ZnCl_2$ (black curve) exhibited the lowest capacitance (24.64 F g^{-1}). Overall, the capacitance ranking followed the order: DES–KI > DES–Gly > DES–ACN > PEG–$ZnCl_2$. These results establish a quantitative comparison with literature-reported DES electrolytes, highlighting the tunability of electrochemical properties through additive incorporation. The KI-containing DES exhibited enhanced electrochemical performance, achieving an ionic conductivity of 0.052 mS cm^{-1} and a specific capacitance of 41.6 F g^{-1}. These values are comparable to or slightly higher than those reported for ultrasonication-synthesized DES systems. For instance, John *et al*. [61] observed improved conductivity and uniformity in ultrasonically synthesized DESs compared to conventionally prepared systems, albeit with lower conductivity. Zdolšek *et al*. [62] developed Mn_3O_4@N-doped carbon electrodes via an ultrasound-assisted DES route, achieving capacitances below 35 F g^{-1} under comparable conditions. Lu *et al*. [63] enhanced redox activity in a DES-based non-aqueous redox flow battery using ultrasonication and magnetic fields, but remained limited by viscosity-driven conductivity constraints. Shan *et al*. [64] used a DES-assisted electrochemical–ultrasonic exfoliation method for MXene production without evaluating electrolyte potential. Wu *et al*. [48] emphasized the persistent trade-off between viscosity and conductivity in DES electrolytes, a challenge mitigated here through KI incorporation and ultrasonic homogenization.

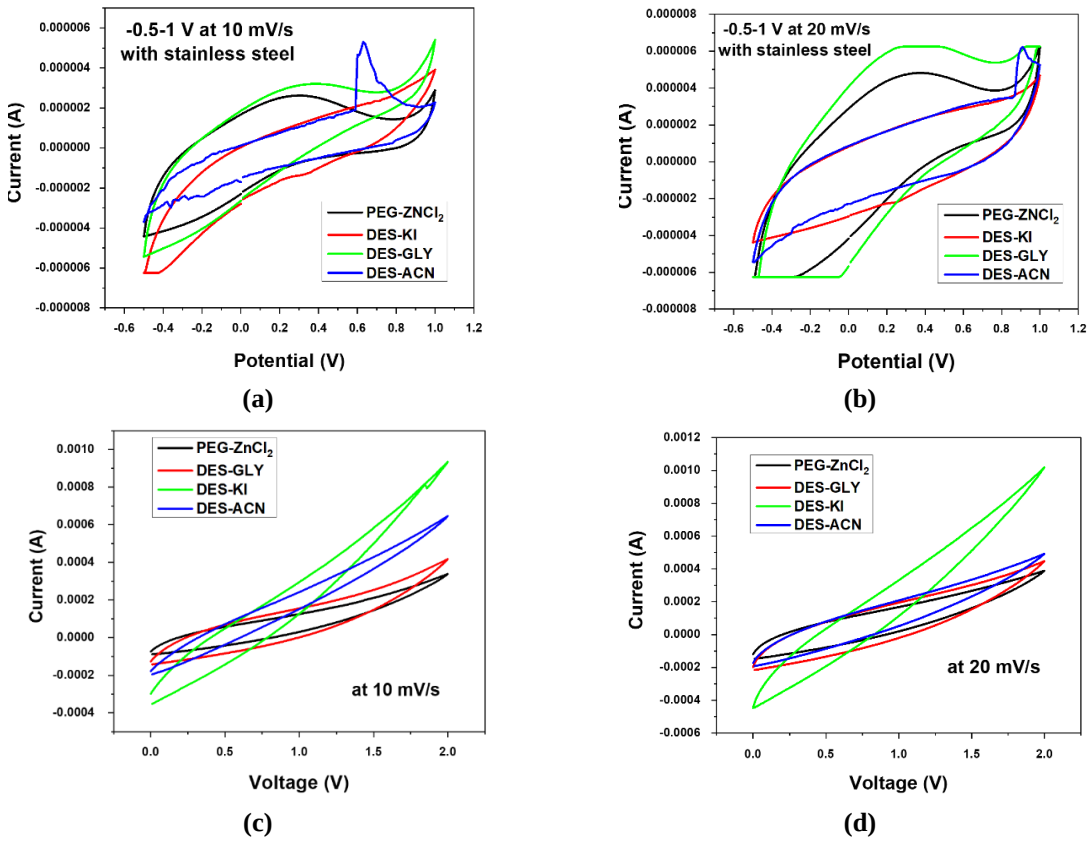

Figure 6. (a) Cyclic voltammograms of DESs with stainless steel electrodes at 10 mV s^{-1} showing redox activity; **(b)** corresponding CVs at 20 mV s^{-1} highlighting scan rate effects; **(c)** CVs with activated carbon electrodes (ACE) at 10 mV s^{-1} indicating capacitive behavior; **(d)** CVs with ACE at 20 mV s^{-1} demonstrating enhanced current response and quasi-reversible electrochemical characteristics.

Similarly, Lien *et al*. [35] improved DES conductivity by adding co-solvents such as water or acetonitrile, whereas the present system achieves comparable conductivity without dilution, relying instead on redox-active additive integration. Tsai *et al*. [52] formulated an

N-methylacetamide–lithium perchlorate DES with DMF/water co-solvents, attaining a wide ESW (2.2 V) and a specific capacitance of 41.9 F g^{-1} at 25°C. While capacitance values are similar, the PEG–$ZnCl_2$–KI formulation presented here achieves comparable performance through a simpler, co-solvent-free ultrasonication process.

3.6. Validation of high conductivity in KI despite high viscosity.

EIS was employed to investigate the charge transport and capacitive characteristics of the synthesized DES systems. The Nyquist plots (Figure 7a–d) for all electrolytes display slanted lines without semicircular regions, indicative of dominant capacitive behavior and minimal charge transfer resistance (R_{ct}) at the electrode–electrolyte interface. This confirms that ionic conduction and double-layer capacitance processes prevail over faradaic reactions [65]. The low-frequency linear regions further reflect efficient ion diffusion and mobility within the DES matrices. Among the tested systems, DES–KI exhibited the highest ionic conductivity, measured as 0.052 mS cm^{-1} by EIS (Figure 7b). This enhancement is attributed to increased ionic concentration arising from KI dissociation into K^+ and I^- ions, which improves charge transport pathways. PEG–$ZnCl_2$ and DES–Gly displayed moderate conductivities of 0.028 mS cm^{-1} (Figure 7a) and 0.026 mS cm^{-1} (Figure 7c), respectively, both maintaining clear capacitive behavior. DES–Gly achieved a slightly higher specific capacitance (38.48 F g^{-1}) than PEG–$ZnCl_2$ (24.64 F g^{-1}), likely due to the hydroxyl-rich glycerol promoting stronger ionic interactions. DES–ACN showed the lowest conductivity (0.022 mS cm^{-1}; Figure 7d) and specific capacitance (25 F g^{-1}), consistent with weaker hydrogen bonding and partial disruption of the PEG–$ZnCl_2$ coordination structure.

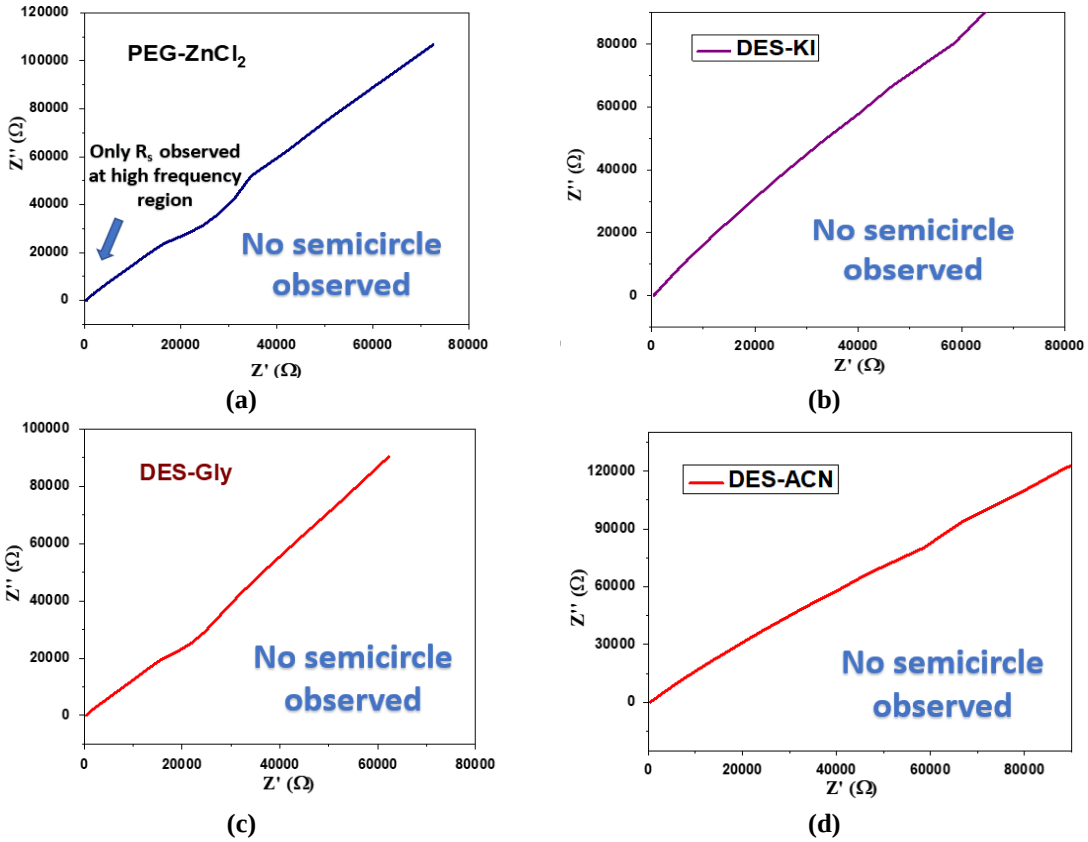

Figure 7. (a) EIS Nyquist plot of PEG–$ZnCl_2$ DES; **(b)** DES–KI; **(c)** DES–Gly; **(d)** DES–ACN recorded with stainless steel electrodes from 0.01 Hz to 1 kHz, showing semicircular and vertical regions indicative of low charge-transfer resistance.

Conductivity values obtained from EIS were in close agreement with direct measurements using a conductivity meter (Table 5). DES–KI again exhibited the highest value (0.060 mS cm^{-1} by meter vs. 0.052 mS cm^{-1} by EIS), despite its relatively high viscosity (917 mPa·s). This suggests that effective ionic dissociation and well-connected conductive pathways compensate for the viscous medium, supporting efficient charge transport. At the same time, previous studies have attributed similar trends to proton transfer through hydrogen-bond networks [66, 67]. The iodide ions further enhance proton mobility through the Grotthuss mechanism, a hopping process in which protons rapidly transfer between hydrogen-bonding sites. These ions stabilize intermediate species such as H_3O^+ (Eigen complex) and $H_5O_2^+$ (Zundel complex), thereby lowering the energy barrier for proton hopping [68,69]. Such mechanisms were not quantitatively analyzed here and therefore warrant further investigation. The conductivity trend followed DES–KI > PEG–$ZnCl_2$ > DES–Gly ≈ DES–ACN, consistent with specific capacitance results. The absence of semicircles in all Nyquist plots confirms low R_{ct}. These findings demonstrate that all DES systems provide stable capacitive characteristics and reliable ionic conduction, with DES–KI showing the most favorable balance between conductivity and interfacial stability. Further studies integrating quantitative transport modeling or molecular simulations could help elucidate the mechanisms underlying ion mobility in these eutectic systems.

Table 5. Viscosity and conductivity of synthesized DES systems were measured using a conductivity meter and calculated from EIS analysis. Data are reported as mean ± standard deviation (n = 3).

DES System	Viscosity (mPa·s)	Conductivity (mS·cm^{-1}) *(Conductivity Meter)*	Conductivity (mS·cm^{-1}) *(EIS Plot)*
PEG–$ZnCl_2$	530 ± 6	0.040 ± 0.002	0.028 ± 0.001
DES–Glycerol	517 ± 5	0.035 ± 0.001	0.026 ± 0.001
DES–ACN	360 ± 4	0.039 ± 0.001	0.022 ± 0.001
DES–KI	917 ± 8	0.060 ± 0.003	0.052 ± 0.002

4. Conclusions

This study demonstrates that DESs synthesized from PEG and $ZnCl_2$, with additives such as KI, glycerol, and ACN, exhibit electrochemical properties suitable for supercapacitor applications. Among the tested systems, DES-KI showed the highest ionic conductivity (0.052 mS cm^{-1}) and specific capacitance (41.6 F g^{-1}), reflecting enhanced ion transport and charge storage capability. PEG-$ZnCl_2$ and DES-ACN also displayed broad electrochemical stability windows and well-defined redox peaks, while DES-Gly exhibited moderate conductivity but strong electrode-electrolyte interactions supported by hydrogen bonding. EIS analysis confirmed predominantly capacitive behavior with low charge-transfer resistance across all systems, correlating well with conductivity and stability trends. Overall, the results highlight the potential of these DESs as environmentally friendly and composition-tunable electrolytes for next-generation energy storage devices. Future research should employ molecular dynamics simulations and scalability assessments to gain deeper insight into ion transport mechanisms and enable practical deployment in large-scale electrochemical systems. However, the present study is limited to experimental electrochemical characterization; quantitative modeling of ion transport mechanisms and viscosity effects is required to validate the proposed interpretations. Future studies should focus on molecular dynamics simulations, scalable synthesis strategies, and long-term electrochemical cycling to further establish the practical viability of these DES-based electrolytes.

Author Contributions

Conceptualization, P.K. and Y.K.; methodology, P.K.; software, P.K.; validation, P.K., Y.K., and K.B.; formal analysis, P.K. and M.V.; investigation, Y.K.; data curation, P.K.; writing—original draft preparation, P.K.; writing—review and editing, P.K.; visualization, M.V.; supervision, K.B. All authors have read and agreed to the published version of the manuscript.

Institutional Review Board Statement

Not applicable.

Informed Consent Statement

Not applicable.

Data Availability Statement

Data supporting the findings of this study are available upon reasonable request from the corresponding author.

Funding

This research received no external funding.

Acknowledgments

Declared none.

Conflicts of Interest

The authors declare no conflict of interest.

Abbreviations

The following abbreviations are used in this manuscript:

Abbreviation	Definition
AC	Activated Carbon
ACN	Acetonitrile
CV	Cyclic Voltammetry
DES	Deep Eutectic Solvent
DSC	Differential Scanning Calorimetry
EDLC	Electrochemical Double-Layer Capacitor
ED–XRF	Energy-Dispersive X-ray Fluorescence
EIS	Electrochemical Impedance Spectroscopy
ESW	Electrochemical Stability Window
FTIR	Fourier Transform Infrared Spectroscopy
GLY	Glycerol
HBA	Hydrogen-Bond Acceptor
HBD	Hydrogen-Bond Donor
I^-	Iodide Ion
K^+	Potassium Ion
KI	Potassium Iodide
PEG	Polyethylene Glycol
PEG–$ZnCl_2$	Polyethylene Glycol–Zinc Chloride Deep Eutectic Solvent
PVDF–HFP	Polyvinylidene Fluoride–Hexafluoropropylene
Rct	Charge-Transfer Resistance

Abbreviation	Definition
SS	Stainless Steel
TGA	Thermogravimetric Analysis
T_{onset}	Onset Decomposition Temperature
$ZnCl_2$	Zinc Chloride
Zn^{2+}	Zinc Ion

References

1. Kumar, P.; Banerjee, K.; Kumar, Y. Tailoring Novel Glycerol-Potassium Iodide Deep Eutectic Solvents: A Comprehensive Investigation of Physical, Structural, and Electrochemical Properties. *J. Mol. Liq.* **2024**, *414*, 126031, https://doi.org/10.1016/j.molliq.2024.126031.
2. Wei, P.; Pan, X.; Chen, C.-Y.; Li, H.-Y.; Yan, X.; Li, C.; Chu, Y.-H.; Yan, B. Emerging Impacts of Ionic Liquids on Eco-Environmental Safety and Human Health. *Chem. Soc. Rev.* **2021**, *50*, 13609–13627, https://doi.org/10.1039/D1CS00946J.
3. Weerasinghe, U.A.; Wu, T.; Chee, P.L.; Yew, P.Y.M.; Lee, H.K.; Loh, X.J.; Dan, K. Deep Eutectic Solvents towards Green Polymeric Materials. *Green Chem.* **2024**, *26*, 8497–8527, https://doi.org/10.1039/D4GC00532E.
4. Zhang, R.; Zhou, H.; Ma, Q.; Li, Z.; Lu, M.; Su, H.; Yang, W.; Xu, Q. Numerical Optimization of Magnetic Field Application Scheme for Deep Eutectic Solvent (DES) Electrolyte Flow Battery. *J. Power Sources* **2023**, *586*, 233683, https://doi.org/10.1016/j.jpowsour.2023.233683.
5. Lim, E.; Yon Pang, J.-S.; Lau, E.V. A Comparative Study of Thermophysical Properties between Choline Chloride-Based Deep Eutectic Solvents and Imidazolium-Based Ionic Liquids. *J. Mol. Liq.* **2024**, *395*, 123895, https://doi.org/10.1016/j.molliq.2023.123895.
6. Freitas, D.S.; Cavaco-Paulo, A.; Silva, C. Enhancing Insights into the Phenomena of Deep Eutectic Solvents. *Sustain. Mater. Technol.* **2024**, *41*, e01039, https://doi.org/10.1016/j.susmat.2024.e01039.
7. Wen, S.; Wang, T.; Zhang, X.; Hu, X.; Wu, Y. Deep Eutectic Solvents Formed by Novel Metal-Based Amino Acid Salt and Dihydric Alcohol for Highly Efficient Capture of CO_2. *J. Environ. Chem. Eng.* **2024**, *12*, 112533, https://doi.org/10.1016/j.jece.2024.112533.
8. Wang, S.; Liu, G.; Wan, W.; Li, X.; Li, J.; Wang, C. Acetamide-Caprolactam Deep Eutectic Solvent-Based Electrolyte for Stable Zn-Metal Batteries. *Adv. Mater.* **2024**, *36*, 2306546, https://doi.org/10.1002/adma.202306546.
9. Perry, S.C.; White, J.; Nandhakumar, I. Template-Free Electrochemical Deposition of Tellurium Nanowires with Eutectic Solvents. *Electrochimica Acta* **2023**, *439*, 141674, https://doi.org/10.1016/j.electacta.2022.141674.
10. Fan, X.; Zhao, Z.; Li, C.; Li, X.; He, Y.; Zhu, M. Deep Eutectic Solvent Intercalation Graphene Oxide with Strong Interfacial Adsorption Capacity towards Efficient Lubrication. *Carbon* **2024**, *216*, 118508, https://doi.org/10.1016/j.carbon.2023.118508.
11. Alhanash, M.; Johansson, P. Tight-Binding Modelling of Deep Eutectic Solvent Based Electrolytes. *Meet. Abstr.* **2023**, *MA2023-02*, 741–741, https://doi.org/10.1149/MA2023-024741mtgabs.
12. Abbott, A.P.; Capper, G.; Davies, D.L.; Rasheed, R.K.; Tambyrajah, V. Novel solvent properties of choline chloride/urea mixtures. *Chem. Commun.* **2003**, 70–71, https://doi.org/10.1039/b210714g.
13. Florindo, C.; Oliveira, F.S.; Rebelo, L.P.N.; Fernandes, A.M.; Marrucho, I.M. Insights into the Synthesis and Properties of Deep Eutectic Solvents Based on Cholinium Chloride and Carboxylic Acids. *ACS Sustainable Chem. Eng.* **2014**, *2*, 2416–2425, https://doi.org/10.1021/sc500439w.
14. Rodriguez Rodriguez, N.; Van Den Bruinhorst, A.; Kollau, L.J.B.M.; Kroon, M.C.; Binnemans, K. Degradation of Deep-Eutectic Solvents Based on Choline Chloride and Carboxylic Acids. *ACS Sustainable Chem. Eng.* **2019**, *7*, 11521–11528, https://doi.org/10.1021/acssuschemeng.9b01378.
15. Sholidodov, M.; Saidentsal, A.; Altunina, L.; Kozlov, V.; Kuvshinov, V.; Stasyeva, L.; Mustafin, R. Chemistry for sustainable development. *Chemistry* **2024**, *32*, 330-337, https://doi.org/10.15372/CSD2024565.
16. Shaibuna, M.; Theresa, L.V.; Sreekumar, K. Neoteric Deep Eutectic Solvents: History, Recent Developments, and Catalytic Applications. *Soft Matter.* **2022**, *18*, 2695–2721, https://doi.org/10.1039/D1SM01797G.

17. Dai, Y.; Witkamp, G.-J.; Verpoorte, R.; Choi, Y.H. Tailoring Properties of Natural Deep Eutectic Solvents with Water to Facilitate Their Applications. *Food Chem.* **2015**, *187*, 14–19, https://doi.org/10.1016/j.foodchem.2015.03.123.
18. Farooq, M.Q.; Abbasi, N.M.; Anderson, J.L. Deep Eutectic Solvents in Separations: Methods of Preparation, Polarity, and Applications in Extractions and Capillary Electrochromatography. *J. Chromatogr. A* **2020**, *1633*, 461613, https://doi.org/10.1016/j.chroma.2020.461613.
19. Nam, M.W.; Zhao, J.; Lee, M.S.; Jeong, J.H.; Lee, J. Enhanced Extraction of Bioactive Natural Products Using Tailor-Made Deep Eutectic Solvents: Application to Flavonoid Extraction from Flos Sophorae. *Green Chem.* **2015**, *17*, 1718–1727, https://doi.org/10.1039/C4GC01556H.
20. Crawford, D.E.; Wright, L.A.; James, S.L.; Abbott, A.P. Efficient Continuous Synthesis of High Purity Deep Eutectic Solvents by Twin Screw Extrusion. *Chem. Commun.* **2016**, *52*, 4215–4218, https://doi.org/10.1039/C5CC09685E.
21. Singh, B.S.; Lobo, H.R.; Pinjari, D.V.; Jarag, K.J.; Pandit, A.B.; Shankarling, G.S. Ultrasound and Deep Eutectic Solvent (DES): A Novel Blend of Techniques for Rapid and Energy Efficient Synthesis of Oxazoles. *Ultrason. Sonochem.* **2013**, *20*, 287–293, https://doi.org/10.1016/j.ultsonch.2012.06.003.
22. Rutkowska, M.; Namieśnik, J.; Konieczka, P. Chapter 10 - Ultrasound-Assisted Extraction. In The Application of Green Solvents in Separation Processes, Pena-Pereira, F., Tobiszewski, M., Eds.; Elsevier: **2017**; pp. 301-324, https://doi.org/10.1016/B978-0-12-805297-6.00010-3.
23. Calvo-Flores, F.G.; Mingorance-Sánchez, C. Deep Eutectic Solvents and Multicomponent Reactions: Two Convergent Items to Green Chemistry Strategies. *ChemistryOpen* **2021**, *10*, 815–829, https://doi.org/10.1002/open.202100137.
24. Martín, M.I.; García-Díaz, I.; Rodríguez, M.L.; Gutiérrez, M.C.; Del Monte, F.; López, F.A. Synthesis and Properties of Hydrophilic and Hydrophobic Deep Eutectic Solvents via Heating-Stirring and Ultrasound. *Molecules* **2024**, *29*, 3089, https://doi.org/10.3390/molecules29133089.
25. Santana, A.P.R.; Mora-Vargas, J.A.; Guimarães, T.G.S.; Amaral, C.D.B.; Oliveira, A.; Gonzalez, M.H. Sustainable Synthesis of Natural Deep Eutectic Solvents (NADES) by Different Methods. *J. Mol. Liq.* **2019**, *293*, 111452, https://doi.org/10.1016/j.molliq.2019.111452.
26. Długosz, O.; Banach, M. Green Methods for Obtaining Deep Eutectic Solvents (DES). *J. Clean. Prod.* **2024**, *434*, 139914, https://doi.org/10.1016/j.jclepro.2023.139914.
27. Yahaya, N.; Mohamed, A.H.; Sajid, M.; Zain, N.N.M.; Liao, P.-C.; Chew, K.W. Deep Eutectic Solvents as Sustainable Extraction Media for Extraction of Polysaccharides from Natural Sources: Status, Challenges and Prospects. *Carbohydr. Polym.* **2024**, *338*, 122199, https://doi.org/10.1016/j.carbpol.2024.122199.
28. Socas-Rodríguez, B.; Santana-Mayor, Á.; Herrera-Herrera, A.V.; Rodríguez-Delgado, M.Á. Chapter 5 - Deep eutectic solvents. In Green Sustainable Process for Chemical and Environmental Engineering and Science, Inamuddin, Asiri, A.M., Kanchi, S., Eds.; Elsevier: **2020**; pp. 123-177, https://doi.org/10.1016/B978-0-12-817386-2.00005-6.
29. Singh, M.B.; Kumar, V.S.; Chaudhary, M.; Singh, P. A Mini Review on Synthesis, Properties and Applications of Deep Eutectic Solvents. *J. Indian Chem. Soc.* **2021**, *98*, 100210, https://doi.org/10.1016/j.jics.2021.100210.
30. Długosz, O. Natural Deep Eutectic Solvents in the Synthesis of Inorganic Nanoparticles. *Materials* **2023**, *16*, 627, https://doi.org/10.3390/ma16020627.
31. Zainal-Abidin, M.H.; Hayyan, M.; Ngoh, G.C.; Wong, W.F.; Looi, C.Y. Emerging Frontiers of Deep Eutectic Solvents in Drug Discovery and Drug Delivery Systems. *J. Control. Release* **2019**, *316*, 168–195, https://doi.org/10.1016/j.jconrel.2019.09.019.
32. Ijardar, S.P.; Singh, V.; Gardas, R.L. Revisiting the Physicochemical Properties and Applications of Deep Eutectic Solvents. *Molecules* **2022**, *27*, 1368, https://doi.org/10.3390/molecules27041368.
33. Cruz, H.; Jordao, N.; Pinto, A.L.; Dionisio, M.; Neves, L.A.; Branco, L.C. Alkaline Iodide-Based Deep Eutectic Solvents for Electrochemical Applications. *ACS Sustainable Chem. Eng.* **2020**, *8*, 10653-10663, https://doi.org/10.1021/acssuschemeng.9b06733.
34. Yang, X.; Feng, W.; Wang, X.; Mu, J.; Liu, C.; Wu, X.; Zhou, P.; Zhou, J.; Zhuo, S. Structural Adjustment on Fluorinated Graphene and Their Supercapacitive Properties in KI-Additive Electrolyte. *J. Electroanal. Chem.* **2023**, *928*, 117010, https://doi.org/10.1016/j.jelechem.2022.117010.
35. Lien, C.-W.; Vedhanarayanan, B.; Chen, J.-H.; Lin, J.-Y.; Tsai, H.-H.; Shao, L.-D.; Lin, T.-W. Optimization of Acetonitrile/Water Content in Hybrid Deep Eutectic Solvent for Graphene/MoS2 Hydrogel-Based Supercapacitors. *Chem. Eng. J.* **2021**, *405*, 126706, https://doi.org/10.1016/j.cej.2020.126706.

36. Huang, W.; Yan, X.; Xiong, Y.; Guo, Q.; Zhang, X.; Huang, F.; Shi, H.; Ge, X. Screening the Deep Eutectic Electrolytes for Supercapacitors with Alleviated Self-Discharge. *Energy Adv.* **2023**, *2*, 1935–1941, https://doi.org/10.1039/D3YA00390F.
37. Zhu, W.; Zheng, X. Biodegradable Lubricant with High-Temperature and Ionic-Contamination Resistance: Deep Eutectic Solvent ChCl-PEG. *ACS Omega* **2022**, *7*, 38380–38388, https://doi.org/10.1021/acsomega.2c03227.
38. Sedghamiz, M.A.; Raeissi, S. Physical Properties of Deep Eutectic Solvents Formed by the Sodium Halide Salts and Ethylene Glycol, and Their Mixtures with Water. *J. Mol. Liq.* **2018**, *269*, 694–702, https://doi.org/10.1016/j.molliq.2018.08.045.
39. Negi, T.; Kumar, A.; Sharma, S.K.; Rawat, N.; Saini, D.; Sirohi, R.; Prakash, O.; Dubey, A.; Dutta, A.; Shahi, N.C. Deep Eutectic Solvents: Preparation, Properties, and Food Applications. *Heliyon* **2024**, *10*, e28784, https://doi.org/10.1016/j.heliyon.2024.e28784.
40. Hsieh, Y.-H.; Li, Y.; Pan, Z.; Chen, Z.; Lu, J.; Yuan, J.; Zhu, Z.; Zhang, J. Ultrasonication-Assisted Synthesis of Alcohol-Based Deep Eutectic Solvents for Extraction of Active Compounds from Ginger. *Ultrason. Sonochem.* **2020**, *63*, 104915, https://doi.org/10.1016/j.ultsonch.2019.104915.
41. Almeida, J.; Craveiro, R.; Faria, P.; Silva, A.S.; Mateus, E.P.; Barreiros, S.; Paiva, A.; Ribeiro, A.B. Electrodialytic removal of tungsten and arsenic from secondary mine resources — Deep eutectic solvents enhancement. *Sci. Total Environ.* **2020**, *710*, 136364, https://doi.org/10.1016/j.scitotenv.2019.136364.
42. da Cruz, M.G.A.; Rodrigues, B.V.M.; Ristic, A.; Budnykb, S.; Das, S.; Slabon, A. On the Product Selectivity in the Electrochemical Reductive Cleavage of Lignin Model Compounds. *Arxiv* **2021**, *15*, 153-161, https://doi.org/10.48550/ARXIV.2108.09771.
43. Schulz, A.; Lunkenheimer, P.; Loidl, A. Ionic Conductivity of a Lithium-Doped Deep Eutectic Solvent: Glass Formation and Rotation–Translation Coupling. *J. Phys. Chem. B* **2024**, *128*, 3454–3462, https://doi.org/10.1021/acs.jpcb.4c00412.
44. Malfait, B.; Jani, A.; Morineau, D. Confining Deep Eutectic Solvents in Nanopores: Insight into Thermodynamics and Chemical Activity. *J. Mol. Liq.* **2022**, *349*, 118488, https://doi.org/10.1016/j.molliq.2022.118488.
45. Nam, N.N.; Do, H.D.K.; Trinh, K.T.L.; Lee, N.Y. Design Strategy and Application of Deep Eutectic Solvents for Green Synthesis of Nanomaterials. *Nanomaterials* **2023**, *13*, 1164, https://doi.org/10.3390/nano13071164.
46. Deng, R.; Gao, M.; Zhang, B.; Zhang, Q. Solvent-Mediated Synthesis of Functional Powder Materials from Deep Eutectic Solvents for Energy Storage and Conversion: A Review. *Adv. Energy Mater.* **2024**, *14*, 2303707, https://doi.org/10.1002/aenm.202303707.
47. Khalid, A.; Tahir, S.; Khalid, A.R.; Hanif, M.A.; Abbas, Q.; Zahid, M. Breaking New Grounds: Metal Salts Based-Deep Eutectic Solvents and Their Applications- a Comprehensive Review. *Green Chem.* **2024**, *26*, 2421–2453, https://doi.org/10.1039/d3gc04112c.
48. Wu, J.; Liang, Q.; Yu, X.; Lü, Q.; Ma, L.; Qin, X.; Chen, G.; Li, B. Deep Eutectic Solvents for Boosting Electrochemical Energy Storage and Conversion: A Review and Perspective. *Adv. Funct. Mater.* **2021**, *31*, 2011102, https://doi.org/10.1002/adfm.202011102.
49. He, L.; Chen, L.; Zheng, B.; Zhou, H.; Wang, H.; Li, H.; Zhang, H.; Xu, C.C.; Yang, S. Deep Eutectic Solvents for Catalytic Biodiesel Production from Liquid Biomass and Upgrading of Solid Biomass into 5-Hydroxymethylfurfural. *Green Chem.* **2023**, *25*, 7410–7440, https://doi.org/10.1039/d3gc02816j.
50. Abbasi, N.M.; Farooq, M.Q.; Anderson, J.L. Investigating the Effect of Systematically Modifying the Molar Ratio of Hydrogen Bond Donor and Acceptor on Solvation Characteristics of Deep Eutectic Solvents Formed Using Choline Chloride Salt and Polyalcohols. *J. Chromatogr. A* **2022**, *1667*, 462871, https://doi.org/10.1016/j.chroma.2022.462871.
51. Mahanta, U.; Choudhury, S.; Venkatesh, R.P.; SarojiniAmma, S.; Ilangovan, S.A.; Banerjee, T. Ionic-Liquid-Based Deep Eutectic Solvents as Novel Electrolytes for Supercapacitors: COSMO-SAC Predictions, Synthesis, and Characterization. *ACS Sustainable Chem. Eng.* **2020**, *8*, 372–381, https://doi.org/10.1021/acssuschemeng.9b05596.
52. Tsai, Y.-R.; Vedhanarayanan, B.; Chen, T.-Y.; Lin, Y.-C.; Lin, J.-Y.; Ji, X.; Lin, T.-W. A Tailor-Made Deep Eutectic Solvent for 2.2 V Wide Temperature-Tolerant Supercapacitors via Optimization of N,N-Dimethylformamide/Water Co-Solvents. *J. Power Sources* **2022**, *521*, 230954, https://doi.org/10.1016/j.jpowsour.2021.230954.

53. Teng, Z.; Han, K.; Li, J.; Gao, Y.; Li, M.; Ji, T. Ultrasonic-Assisted Preparation and Characterization of Hierarchical Porous Carbon Derived from Garlic Peel for High-Performance Supercapacitors. *Ultrason. Sonochem.* **2020**, *60*, 104756, https://doi.org/10.1016/j.ultsonch.2019.104756.
54. Li, W.; Chen, J.; Zhao, J.; Zhang, J.; Zhu, J. Application of Ultrasonic Irradiation in Preparing Conducting Polymer as Active Materials for Supercapacitor. *Mater. Lett.* **2005**, *59*, 800–803, https://doi.org/10.1016/j.matlet.2004.11.024.
55. Strmcnik, D.; Li, D.; Lopes, P.P.; Tripkovic, D.; Kodama, K.; Stamenkovic, V.R.; Markovic, N.M. When Small Is Big: The Role of Impurities in Electrocatalysis. *Top Catal.* **2015**, *58*, 1174–1180, https://doi.org/10.1007/s11244-015-0492-8.
56. Ibrahim, R.K.; Hayyan, M.; AlSaadi, M.A.; Ibrahim, S.; Hayyan, A.; Hashim, M.A. Physical Properties of Ethylene Glycol-Based Deep Eutectic Solvents. *J. Mol. Liq.* **2019**, *276*, 794–800, https://doi.org/10.1016/j.molliq.2018.12.032.
57. Seki, S.; Hayamizu, K.; Tsuzuki, S.; Takahashi, K.; Ishino, Y.; Kato, M.; Nozaki, E.; Watanabe, H.; Umebayashi, Y. Density, Viscosity, Ionic Conductivity, and Self-Diffusion Coefficient of Organic Liquid Electrolytes: Part I. Propylene Carbonate + Li, Na, Mg and Ca Cation Salts. *J. Electrochem. Soc.* **2018**, *165*, A542–A546, https://doi.org/10.1149/2.0081803jes.
58. Ghaedi, H.; Ayoub, M.; Sufian, S.; Lal, B.; Uemura, Y. Thermal Stability and FT-IR Analysis of Phosphonium-Based Deep Eutectic Solvents with Different Hydrogen Bond Donors. *J. Mol. Liq.* **2017**, *242*, 395–403, https://doi.org/10.1016/j.molliq.2017.07.016.
59. Dollimore, D.; Evans, T.A.; Lee, Y.F.; Pee, G.P.; Wilburn, F.W. The Significance of the Onset and Final Temperatures in the Kinetic Analysis of TG Curves. *Thermochim. Acta* **1992**, *196*, 255–265, https://doi.org/10.1016/0040-6031(92)80089-F.
60. Balducci, A. Electrolytes for High Voltage Electrochemical Double Layer Capacitors: A Perspective Article. *J. Power Sources* **2016**, *326*, 534–540, https://doi.org/10.1016/j.jpowsour.2016.05.029.
61. Gutiérrez, M.C.; Ferrer, M.L.; Mateo, C.R.; del Monte, F. Freeze-Drying of Aqueous Solutions of Deep Eutectic Solvents: A Suitable Approach to Deep Eutectic Suspensions of Self-Assembled Structures. *Langmuir* **2009**, *25*, 5509–5515, https://doi.org/10.1021/la900552b.
62. Zdolšek, N.; Perović, I.; Brković, S.; Tasić, G.; Milović, M.; Vujković, M. Deep Eutectic Solvent for Facile Synthesis of Mn_3O_4@N-Doped Carbon for Aqueous Multivalent-Based Supercapacitors: New Concept for Increasing Capacitance and Operating Voltage. *Materials* **2022**, *15*, 8540, https://doi.org/10.3390/ma15238540.
63. Lu, L.; Zhou, H.; Sun, P.; Shen, X.; Li, Z.; Ma, Q.; Su, H.; Xu, Q. Synergistic Effect of Ultrasonic and Magnetic Fields on the Performance of Non-Aqueous Iron-Vanadium Redox Flow Battery with Deep Eutectic Solvent Electrolyte. *J. Energy Storage* **2023**, *63*, 107036, https://doi.org/10.1016/j.est.2023.107036.
64. Shan, Q.; Ding, Q.; Wu, W. Preparation of Antioxidative MXene by Deep Eutectic Solvent-Assisted Electrochemical Ultrasonic Composite Exfoliation and Its Application in Flexible Solid-State Supercapacitors. *Ind. Eng. Chem. Res.* **2023**, *62*, 9492–9502, https://doi.org/10.1021/acs.iecr.3c00989.
65. Lazanas, A.Ch.; Prodromidis, M.I. Electrochemical Impedance Spectroscopy─A Tutorial. *ACS Meas. Sci. Au* **2023**, *3*, 162–193, https://doi.org/10.1021/acsmeasuresciau.2c00070.
66. Aziz, M.F.; Buraidah, M.H.; Careem, M.A.; Arof, A.K. PVA Based Gel Polymer Electrolytes with Mixed Iodide Salts (K^+I^- and $Bu_4N^+I^-$) for Dye-Sensitized Solar Cell Application. *Electrochim. Acta* **2015**, *182*, 217–223, https://doi.org/10.1016/j.electacta.2015.09.035.
67. Aziz, S.B.; Asnawi, A.S.F.M.; Abdulwahid, R.T.; Ghareeb, H.O.; Alshehri, S.M.; Ahamad, T.; Hadi, J.M.; Kadir, M.F.Z. Design of Potassium Ion Conducting PVA Based Polymer Electrolyte with Improved Ion Transport Properties for EDLC Device Application. *J. Mater. Res. Technol.* **2021**, *13*, 933–946, https://doi.org/10.1016/j.jmrt.2021.05.017.
68. Li, W.-H.; Deng, W.-H.; Wang, G.-E.; Xu, G. Conductive MOFs. *EnergyChem* **2020**, *2*, 100029, https://doi.org/10.1016/j.enchem.2020.100029.
69. Maiyelvaganan, K.R.; Kamalakannan, S.; Shanmugan, S.; Prakash, M.; Coudert, F.-X.; Hochlaf, M. Identification of a Grotthuss Proton Hopping Mechanism at Protonated Polyhedral Oligomeric Silsesquioxane (POSS) – Water Interface. *J. Colloid Interface Sci.* **2022**, *605*, 701–709, https://doi.org/10.1016/j.jcis.2021.07.115.

Publisher's Note & Disclaimer